

# Scan-Adaptive MRI Undersampling Using Neighbor-based Optimization (SUNO)

Siddhant Gautam, *Student Member, IEEE*, Angqi Li, Nicole Seiberlich, Jeffrey A. Fessler, *Fellow, IEEE*, and Saiprasad Ravishankar, *Senior Member, IEEE*

**Abstract**— Accelerated MRI involves collecting partial  $k$ -space measurements to reduce acquisition time, patient discomfort, and motion artifacts, and typically uses regular undersampling patterns or hand-designed schemes. Recent works have studied population-adaptive sampling patterns that are learned from a group of patients (or scans) based on population-specific metrics. However, such a general sampling pattern can be sub-optimal for any specific scan since it may lack scan or slice adaptive details. To overcome this issue, we propose a framework for jointly learning scan-adaptive Cartesian undersampling patterns and a corresponding reconstruction model from a training set. We use an alternating algorithm for learning the sampling patterns and reconstruction model where we use an iterative coordinate descent (ICD) based offline optimization of scan-adaptive  $k$ -space sampling patterns for each example in the training set. A nearest neighbor search is then used to select the scan-adaptive sampling pattern at test time from initially acquired low-frequency  $k$ -space information. We applied the proposed framework (dubbed SUNO) to the fastMRI multi-coil knee and brain datasets, demonstrating improved performance over currently used undersampling patterns at both  $4\times$  and  $8\times$  acceleration factors in terms of both visual quality and quantitative metrics. The code for the proposed framework is available at <https://github.com/sidgautam95/adaptive-sampling-mri-suno>.

**Index Terms**— Magnetic Resonance Imaging, sampling pattern optimization, deep learning, image reconstruction, iterative coordinate descent, nearest neighbor search.

## I. INTRODUCTION

Magnetic Resonance Imaging (MRI) is a widely used non-invasive biomedical imaging technology that allows visualization of both anatomical structures and physiological functions. Some of its benefits include a lack of ionizing radiation and excellent soft-tissue contrast. MRI scanners sequentially

collect measurements in the time (or spatial frequency) domain (known as  $k$ -space), from which an image is reconstructed. The scanner must sample numerous  $k$ -space points in order to estimate an image with a clinically appropriate spatial resolution, which causes the acquisition process to be slow and expensive. Accelerating MRI scans reduces acquisition time, reduces patient discomfort, increases scaling throughput, and reduces motion artifacts. Such acceleration often requires choosing an appropriate undersampling pattern or trajectory along with a reconstruction model that enables accurate recovery from reduced measurements.

Some of the earliest approaches for accelerating MR imaging included pulse sequence and  $k$ -space trajectory design [1]–[3] and parallel imaging [4]–[6], which exploits the spatial information available when using an array of receiver coils. Parallel imaging offers hardware-based acceleration but often suffers from increased noise and imperfect artifact correction at higher undersampling rates. It is limited to smaller acceleration factors because of imperfect artifact correction and higher noise at higher acceleration rates.

Compressed sensing (CS) [7], [8] has been widely used to enable the reconstruction of MR images from a reduced set of measurements. Traditional MRI follows the Nyquist-Shannon theorem, requiring dense sampling in  $k$ -space. However, according to CS theory, the  $k$ -space sampling can be done at sub-Nyquist rates and the image can be reconstructed using prior knowledge of sparsity in some transform domain [8]–[11] when the sampling operator and sparsity basis are sufficiently incoherent. Some of the widely used undersampling patterns in CS-MRI include variable density [12], Poisson-disc [13], combined variable density and Poisson disc [14], and equispaced Cartesian with skipped lines [15]. Recently, approaches using learned image models for reconstruction have also been explored. These methods include techniques such as synthesis dictionary learning [16]–[19] and transform learning [20], [21].

With the advent of deep learning, convolutional neural networks (CNNs) have achieved tremendous success in reconstructing MR images from undersampled measurements. Some of these approaches have used U-Net architectures [22] by training them in a supervised manner to remove artifacts in aliased images [23]. Similarly, variational networks have been used to solve the image reconstruction problem for accelerated multi-coil MRI by combining neural networks with the MR forward model [24], [25]. Other works in deep

This work was supported by NIH Grant R21 EB030762.

S. Gautam and A. Li are with the Department of Computational Mathematics, Science and Engineering, Michigan State University, East Lansing, MI 48824 USA (e-mail: gautamsi@msu.edu; liangq1@msu.edu).

N. Seiberlich is with the Department of Radiology, University of Michigan, Ann Arbor, MI 48109 USA (e-mail: nse@med.umich.edu).

J. A. Fessler is with the Department of Electrical and Computer Engineering and Department of Biomedical Engineering, University of Michigan, Ann Arbor, MI 48109 USA (e-mail: fessler@umich.edu).

S. Ravishankar is with the Department of Computational Mathematics, Science and Engineering and the Department of Biomedical Engineering, Michigan State University, East Lansing, MI 48824 USA (e-mail: ravisha3@msu.edu).

learning-based MRI reconstruction include ADMM-Net [26] and GANs [27]. Recently, MoDL [28] has become quite popular in solving the MRI reconstruction problem in which the MRI forward model is used within a data consistency term, and a CNN reconstructor is used as a denoiser to regularize the reconstruction.

One of the first works to optimize MRI undersampling patterns used training  $k$ -space data and reconstruction error as the training loss to optimize a single pattern over training scans [29]. Subsequent work on sampling optimization designed adaptive sampling patterns using the power spectra of the reference  $k$ -space data [30], [31] or the energy preserving sampling method [32]. Statistical experiment design techniques for MRI sampling prediction were proposed that used the Cramer-Rao lower bound [33], [34]. Later, the greedy algorithm and its variations were used to learn a single population-adaptive sampling pattern over a training set of images with a specific choice of reconstruction method [35], [36]. Since these approaches learn the undersampling pattern using greedy algorithms over a large number of images, the computational cost involved is high and it scales quadratically with the number of lines in the mask. To avoid this, a stochastic version of the greedy mask learning algorithm was proposed that resolved the scaling issues of the previous greedy approaches [37].

Recently, deep learning approaches were proposed that jointly learn a sampling pattern and a corresponding trained reconstruction network [38]–[44]. LOUPE [38] and its multi-coil extension [39] determines the probability of sampling each pixel or row/column in the  $k$ -space domain. Its underlying parameters are learned jointly with those of the reconstructor (U-Net). Similarly, J-MoDL [40] jointly learns an MoDL reconstruction network and a sampling pattern whose parameters are optimized separately along the row and column directions. MNet [44] also explored jointly training a reconstruction network and a CNN-based sampler to predict the undersampling pattern directly from low-frequency  $k$ -space information. Bias-accelerated subset selection (BASS) [42], [43], a subset selection method for learning sampling patterns, was proposed for parallel MRI applications, which gives a fast way to learn sampling patterns. AutoSamp [45] is one of the recent deep learning methods proposed for joint optimization of sampling patterns and reconstruction for 3D MRI that uses variational information maximization.

Sequential decision processes have also been applied to undersampling prediction where they sequentially learn MRI sampling patterns using reinforcement learning. In these problems, the sampling optimization is formulated as a partially observable Markov decision process (POMDP) [46], [47]. Subsequent works used a reconstruction model trained simultaneously with a sampler that predicts sampling patterns sequentially [48]. These works can be divided into the ones predicting Cartesian undersampling patterns [38], [42]–[45], [48] and the ones learning non-Cartesian patterns [40]. Other recent works for learning non-Cartesian sampling trajectories include PILOT [49], SPARKLING [50], [51], BJORK [52], and SNOPY [53].

One limitation of the more common population-adaptive

approaches [35], [38], [40], [42], [43] is that they learn a sampling pattern suited to the entire dataset rather than to individual scans. Implementing scan-adaptive sampling prediction could potentially enhance sampling efficiency by leveraging key slice or image specific features and thus improve reconstruction performance compared to population-adaptive methods. The population-adaptive designs can be learned off-line, whereas scan-specific sampling patterns must be determined rapidly while the subject is in the scanner, after collecting some preliminary  $k$ -space data.

This paper proposes a framework for jointly learning scan-adaptive 1D Cartesian undersampling patterns and a reconstruction model for multi-coil MRI on a training dataset. Our algorithm alternately estimates a reconstructor and a collection of sampling patterns from training data. We use a sampling optimization algorithm based on iterative coordinate descent to yield improved sampling patterns on training data and use the nearest neighbor search to determine such patterns at test time based on acquired low-frequency  $k$ -space. Our results show that the scan-adaptive Cartesian sampling patterns yield better reconstruction quality in terms of NRMSE, SSIM [54], and PSNR metrics, compared to existing baselines for multi-coil MRI. Moreover, at test time, we also explored efficiently learning local (scan-adaptive) reconstruction networks from small clusters in the training set for each test image. The network is trained with images that are in the local neighborhood of the initial test reconstruction [55]. This paper builds upon our previous short conference work [56] and extends it to higher acceleration factors and learns undersampling patterns over different anatomies. We also present results with scan-adaptive reconstructors along with extended comparisons with several baselines.

The rest of this paper is organized as follows. Section II discusses the details of the MRI forward model, deep learning-based reconstruction, and the details of our proposed training framework that alternates between optimizing a reconstructor and updating scan-adaptive sampling patterns on a training set. Section III discusses the details of training datasets and implementation details. Section IV presents the results of applying our approach to the fastMRI dataset and compares it with existing baselines. We also provide ablation studies on our sampling pattern optimization algorithm. Section V provides a summary of our findings and possible new directions for future work; further conclusions are provided in Section VI.

## II. METHODS

### A. Multi-coil MRI Reconstruction

In multi-coil MRI, the goal is to recover the underlying MR image  $\mathbf{x} \in \mathbb{C}^n$  from a set of undersampled multi-coil measurements  $\mathbf{y} \in \mathbb{C}^m$ . The regularized MRI reconstruction problem can be formulated as follows:

$$\min_{\mathbf{x}} \|\mathbf{M}\mathbf{A}\mathbf{x} - \mathbf{y}\|_2^2 + \lambda\mathcal{R}(\mathbf{x}) \quad (1)$$

Here,  $\mathbf{M}$  is an operator that subsamples  $k$ -space,  $\mathbf{A} = \mathbf{F}\mathbf{S}$  is the fully sampled MRI measurement operator and  $\mathcal{R}(\mathbf{x})$  is a regularizer.  $\mathbf{F}$  is the 2D Fourier transform operator and  $\mathbf{S}$  encodes the sensitivity maps of the receiver coils. The

regularizer  $\mathcal{R}(\mathbf{x})$  typically captures assumed properties of the image and can take on various forms such as total variation, or low-rank or transform-domain sparsity penalties.

Recently, deep learning has become an increasingly powerful tool for solving MRI reconstruction problems. These methods have the advantage that they do not need hand-crafted regularizers. In this paper, we leverage two such deep learning techniques that have been proposed for solving MRI reconstruction problems:

- 1) U-Net [22] is a deep convolutional network that has been used to predict the underlying clean image from the aliased image as follows:

$$\hat{\mathbf{x}} = D_{\theta}(\mathbf{A}^H \mathbf{y}), \quad (2)$$

where  $\hat{\mathbf{x}}$  is the reconstructed image and  $D_{\theta}$  is the reconstruction network (U-Net) with learnable parameters  $\theta$ .

- 2) Model-based deep learning (MoDL) [28] combines deep learning priors with physics-based priors to solve the reconstruction problem. The optimization problem in this case is as follows:

$$\hat{\mathbf{x}} = \arg \min_{\mathbf{x}} \|\mathbf{M}\mathbf{A}\mathbf{x} - \mathbf{y}\|_2^2 + \lambda \|\mathbf{x} - D_{\theta}(\mathbf{x})\|_2^2, \quad (3)$$

where  $D_{\theta}(\mathbf{x})$  is a denoiser (CNN) with learnable parameters  $\theta$ . MoDL tackles (3) by introducing an auxiliary variable  $\mathbf{z}$  and adopting an alternating algorithm as follows:

$$\mathbf{x}_{n+1} = \arg \min_{\mathbf{x}} \|\mathbf{M}\mathbf{A}\mathbf{x} - \mathbf{y}\|_2^2 + \lambda \|\mathbf{x} - \mathbf{z}_n\|_2^2 \quad (4)$$

$$\mathbf{z}_n = D_{\theta}(\mathbf{x}_n) \quad (5)$$

Here,  $\mathbf{x}_{n+1}$  is the estimated image at  $n + 1$  iteration. The alternating scheme is unrolled for a few iterations and the denoising network is trained end to end.

The above expressions are for a fixed or a population-adaptive sampling pattern  $\mathbf{M}$ . However, in this paper, we focus on learning scan-specific sampling patterns  $\{\mathbf{M}_i\}$  instead of a single population-adaptive sampling pattern. In this framework, we first optimize these scan-adaptive masks  $\{\mathbf{M}_i\}$  offline for the training set. Then at test time, these masks are chosen using a nearest neighbor search, as described in a later subsection.

## B. Framework for Jointly Learning Reconstructor and Sampler

This section presents our proposed approach for jointly learning a set of scan-adaptive Cartesian undersampling patterns  $\{\mathbf{M}_i\}$  along with a reconstructor trained to be suitable for all of these undersampling patterns. Using a training set consisting of fully sampled  $k$ -space and corresponding ground truth images, we learn a collection of scan-adaptive sampling masks and a reconstructor from the training data. We formulated the joint optimization problem as follows:

$$\min_{\theta, \mathbf{M}_i \in \mathcal{C}, i \in \{1, \dots, N\}} \sum_{i=1}^N \|f_{\theta}(\mathbf{A}_i^H \mathbf{M}_i \mathbf{y}_i^{\text{full}}) - \mathbf{x}_i^{\text{gt}}\|_2^2, \quad (6)$$

where  $\mathbf{M}_i \in \mathcal{C}$  is the  $i$ th training  $k$ -space subsampling mask that inserts zeros at non-sampled locations,  $\mathbf{y}_i^{\text{full}}$  and  $\mathbf{x}_i^{\text{gt}}$  are the  $i$ th fully sampled multi-coil training  $k$ -space and the corresponding ground truth image, respectively and  $N$  is the number of training images. The set  $\mathcal{C}$  denotes all the 1D Cartesian undersampling patterns with a specified sampling budget.  $\mathbf{A}_i^H$  is the adjoint of the fully sampled multi-coil MRI measurement operator for the  $i$ th training scan, and  $f_{\theta}$  is the reconstruction network trained on the set of sampling patterns  $\{\mathbf{M}_i\}$ .

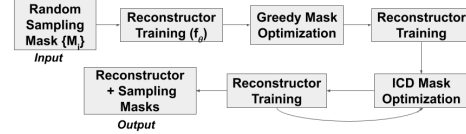


Fig. 1: Alternating framework for mask and reconstructor update during joint training. The first four steps serve to create a good initialization for the mask and reconstructor optimization. The masks could be alternatively initialized with, e.g., population-adapted patterns.

We use the alternating framework shown in Figure 1 to solve this highly challenging optimization problem. The algorithm starts with variable density random sampling (VDERS) masks as an initial guess [8] and alternates between updating a reconstructor and sampling masks until we get a final set of scan-adaptive masks  $\{\mathbf{M}_i\}$  and a reconstruction network  $f_{\theta}$  trained on them. For optimizing the scan-adaptive masks, we initially use a greedy [35] and later our proposed ICD based sampling optimization algorithm. More details of the sampling optimization algorithm are in the next section.

## C. Iterative Coordinate Descent (ICD) based Sampling Optimization

A greedy algorithm was proposed in prior work [35] to optimize high-quality sampling patterns that specifies samples in  $k$ -space that minimize the reconstruction error given a choice of the reconstruction model used. Starting with no sampled lines or only fixed low-frequency lines, at each step of the greedy sampling optimization, the  $k$ -space phase encoding line that gives the lowest reconstruction error is added to a particular sampling mask. The algorithm keeps adding lines until the sampling budget is reached. However, the sampling pattern obtained using the greedy algorithm can be sub-optimal and can be further optimized using an iterative coordinate descent (ICD) based sampling optimization. The proposed iterative coordinate descent (ICD) sampling optimization algorithm further optimizes the greedy mask iteratively by picking one line at a time in the current mask and moving it to the best new location in terms of the reconstruction error and cycling over all lines to move in this manner. Figure 2 shows the schematic of mask updates during various steps of the ICD sampling optimization. The steps of the algorithm are given in detail in Algorithm 1. Thus, the ICD sampling optimization further improves the greedy masks and yields better quality scan-adaptive masks. The optimized masks depend on the choice of the initial mask, the reconstructor used and the metric chosen for the loss function. The ICD sampling optimization

---

**Algorithm 1** Sampling Pattern Optimization
 

---

**Require:** Fully sampled  $k$ -space  $\mathbf{y}^{\text{full}}$  and corresponding forward operator  $\mathbf{A}$ , ground truth image  $\mathbf{x}^{\text{gt}}$ , reconstructor  $f$ , loss function  $L$ , budget  $B$ , number of ICD iterations  $N_{\text{iter}}$ , set of all possible line locations  $\mathbf{S}$ , set of locations of initial sampled lines  $\Omega_{\text{initial}}$ , initial mask  $\mathbf{M}_{\Omega_{\text{initial}}}$

- 1:  $\Omega \leftarrow \Omega_{\text{initial}}$
- 2: **for**  $j = 1 : N_{\text{iter}}$  **do**
- 3:    $\{l_i\}_{i=1}^B \leftarrow$  entries in current  $\Omega$
- 4:   **for**  $i = 1 : B$  **do**
- 5:      $\Omega' = \Omega \setminus l_i$
- 6:      $\Omega \leftarrow \Omega' \cup S^*$  where
 
$$S^* = \arg \min_{S \in \mathbf{S}, S \notin \Omega'} L(\mathbf{x}^{\text{gt}}, f(\mathbf{A}^H \mathbf{M}_{\Omega' \cup S} \mathbf{y}^{\text{full}}))$$

where  $\mathbf{M}_{\Omega' \cup S}$  is the operator sampling along lines at  $\Omega' \cup S$ .

- 7:   **end for**
  - 8: **end for**
  - 9: **return**  $\Omega$
- 

algorithm ensures a monotonic decrease and convergence of the non-negative reconstruction loss (6).

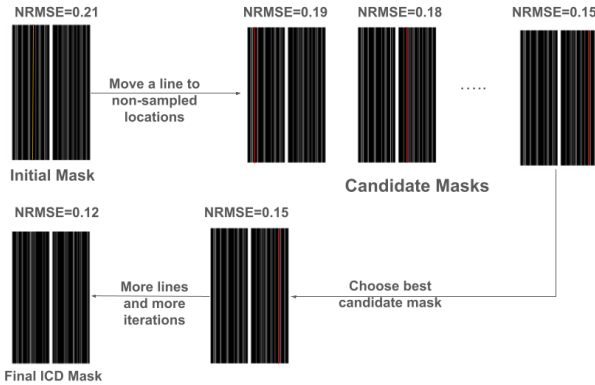


Fig. 2: Schematic of offline iterative coordinate descent (ICD) based sampling pattern optimization.

### D. Neighbor based Sampling Prediction

This subsection describes our approach to predict the sampling pattern from initially acquired  $k$ -space measurements at testing time. Given our set of scan-adaptive sampling patterns obtained from the training process, the task at test time is to estimate the high-frequency lines in  $k$ -space based on initially acquired low-frequency information. We use the nearest neighbor search to predict the sampling pattern from the collection of training scans. The nearest neighbor is found by comparing the adjoint reconstruction of the low-frequency test  $k$ -space and the corresponding low-frequency part of the training  $k$ -space as follows:

$$d_i = d(\mathbf{A}_{\text{test}}^H \mathbf{y}_{\text{test}}^{\text{lf}}, \mathbf{A}_{\text{train}_i}^H \mathbf{y}_{\text{train}_i}^{\text{lf}}), \quad (7)$$

where  $\mathbf{y}_{\text{test}}^{\text{lf}}$  and  $\mathbf{y}_{\text{train}_i}^{\text{lf}}$  are the low-frequency part of testing and training  $k$ -space with zeros at high frequencies.  $\mathbf{A}_{\text{test}}^H$  and

$\mathbf{A}_{\text{train}_i}^H$  are the adjoints of the fully sampled MRI forward operators for the test and  $i$ th training scans, respectively. Different metrics  $d$  can be used to define the nearest neighbors, e.g., Euclidean distance, structural similarity index (SSIM) [54], or normalized cross-correlation. We choose the optimized mask of the nearest neighbor (called the SUNO mask) and use that at test time in the scanner to collect the rest of the measurements.

### E. Local Neighbor-based Reconstructor Training

Adaptive local network training [55] on a set of nearest neighbors can yield better reconstructions compared to a network that is trained globally on all the images in the training set. This is because the local reconstructor is trained on a dataset closely resembling the underlying test image, rather than on a large and diverse training set. As a result, it adapts more effectively to similar or related image features and provides a better fit than a model trained on many unrelated scans. We apply this framework to our SUNO masks and train a local network in addition to a reconstruction network trained globally (i.e., on a large training set). We call the approach with the locally trained reconstruction network ‘‘SUNO-Local’’ and the one with the global network ‘‘SUNO-Global’’ in the rest of the paper. Mathematically, the problem of finding the nearest neighbors for local training can be formulated as:

$$\hat{\mathbf{C}}_{\mathbf{x}} = \arg \min_{C \in \mathcal{C}, |C|=k} \sum_{n \in C} d(\hat{\mathbf{x}}, \mathbf{x}_n), \quad (8)$$

where  $\hat{\mathbf{x}}$  is an initial reconstructed image,  $\mathbf{x}_n$  is the  $n$ th ground truth from the training set and  $d$  is the distance metric used to evaluate neighbors.  $C$  is the set of nearest neighbors with cardinality  $k$  and  $\mathcal{C}$  denotes the set of all such sets with  $k$  elements. We computed the initial reconstructed image MoDL network (that is trained globally) on the test  $k$ -space undersampled by the SUNO mask. Euclidean distance is used as the similarity metric above. The local network is trained for only a few epochs (e.g., using the ADAM optimizer) and a smaller learning rate is used to prevent overfitting on the smaller training set of nearest neighbors.

## III. EXPERIMENTS

### A. Datasets

Our experiments used the fastMRI multi-coil knee and brain datasets [57], [58]. The details for each dataset are as follows:

1) *fastMRI Multi-coil Knee Dataset*: The fastMRI multi-coil knee dataset contains images collected using two different pulse sequences, yielding coronal proton-density weighted images with (PDFS) and without (PD) fat suppression. For our experiments, we used a total of 156 scans (comprising both PD and PDFS scans) and split them into training, validation, and testing sets. From each scan, we discarded the first 10 and last 5 slices due to a lack of identifiable image features, which gave us 1514, 194, and 104 training, validation, and testing slices respectively. Each image was collected using 15 coils of  $k$ -space data with a matrix size of  $640 \times 368$ . We used the ESPIRIT calibration approach [59] to estimate the sensitivity maps from the central 30 lines of  $k$ -space.

2) *fastMRI Multi-coil Brain Dataset*: To test the generalization of our proposed sampling prediction algorithm, we also applied our algorithm on the fastMRI multi-coil brain dataset that consists of FLAIR, T1-weighted, and T2-weighted images. From this dataset, we used a total of 1660 slices for our experiments and split them into 1480, 120, and 60 training, validation, and testing images, respectively. The scans were acquired with a matrix acquisition size of  $640 \times 320$ , and the number of receiver coils varied between 4 and 20 across different scans. The sensitivity maps were estimated using the ESPIRiT calibration approach.

### B. Comparison with Other Undersampling Patterns

We compared our proposed SUNO sampling patterns with low-frequency (LF), variable density random sampling (VDRS) [8], equispaced [15], and trained population adaptive LOUPE [38] masks (all Cartesian). For the LOUPE mask, we modified the publicly available code<sup>1</sup> to the multi-coil setting and trained on the full training set of 1514 slices. We set the slope parameter  $\alpha = 5$  and used a learning rate of  $10^{-3}$  to update the mask parameters. For the LOUPE mask and the other undersampling patterns used, 30 and 15 lines were fixed in the central low-frequency part for  $4\times$  and  $8\times$  undersampling factors, respectively. Figure 3 shows the obtained SUNO mask along with other baseline masks for the knee dataset. Separate undersampling patterns were optimized and estimated using nearest neighbor search for the brain dataset. In this work, we focus only on learning and comparing to other Cartesian undersampling baselines. Table I gives the parameters used inside the sampling optimization algorithm for each acceleration factor. The number of ICD iterations  $N_{iter}$  was set to 1 since the most loss change happens in the first iteration and after that changes are smaller but with increased computation.

Acceleration Factor	$4\times$	$8\times$
Budget ( $B$ )	92	46
Lines fixed at center ( $F$ )	30	15
Lines to be optimized ( $B - F$ )	62	31
Search Space ( $W - F$ )	338	353
No. of ICD iterations $N_{iter}$	1	1

TABLE I: Parameters involved in the sampling optimization algorithm for the fastMRI multi-coil knee dataset with  $k$ -space dimension  $640 \times 368$ . 1/3rd of the lines are fixed at the center of  $k$ -space and the rest of the lines are optimized by the algorithm. The  $k$ -space dimensions for the brain dataset are different ( $640 \times 320$ ), so the rest of the parameters scale accordingly.

### C. Implementation Details

Our algorithms were implemented in Python, using the PyTorch package. We used two-channel U-Net [22] and MoDL [28] as the reconstruction networks to obtain the underlying image from the undersampled  $k$ -space, with the two channels being the real and imaginary parts of the complex image. We used Facebook Research’s implementation of U-Net in the PyTorch framework<sup>2</sup>. For MoDL, we used a deep

<sup>1</sup><https://github.com/caglabahadir/LOUPE>

<sup>2</sup><https://github.com/facebookresearch/fastMRI/blob/main/fastmri/models/unet.py>

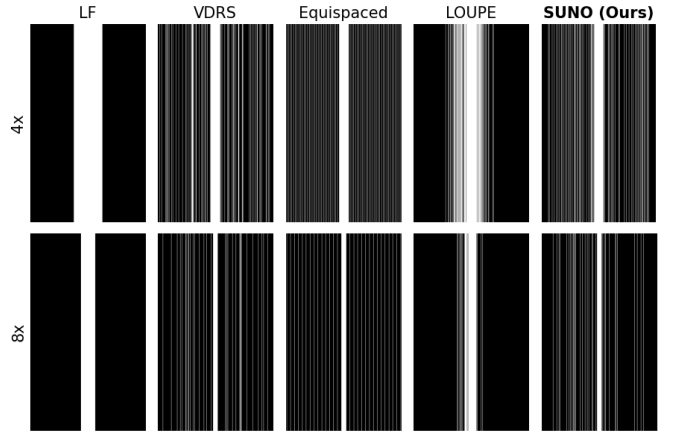


Fig. 3: Comparison of different masks used for reconstruction at a)  $4\times$  and b)  $8\times$  acceleration factors. Masks displayed are: 1) low-frequency (fixed), 2) VDRS (random), 3) Equispaced (fixed), 4) LOUPE (optimized - population adaptive), and 5) SUNO (optimized - scan adaptive).

iterative up-down (DIDN) network [60] as the denoiser inside the training framework. We used 6 unrollings of the denoiser and the conjugate gradient (CG) block. The regularization parameter  $\lambda$  controlling the weighting of the two terms (see Eq.(3)) was set to  $10^2$  and the tolerance for the CG algorithm used was  $10^{-5}$  after tuning them on multiple images. Adam optimizer [61] was used for training the network with a learning rate of  $10^{-3}$ . The networks were trained for 100 epochs with a batch size of 1. All the simulations were performed on an NVIDIA RTX A5000 GPU with 24 GB RAM. For the local training, the MoDL network was trained on the 30 nearest neighbors for 30 epochs. A learning rate of  $10^{-6}$  was used to prevent overfitting in this case since the training set was small. All the training multi-coil  $k$ -space data was undersampled by the ICD mask of the 1st nearest neighbor. All the subsequent testing experiments use a post-trained MoDL on the fixed or optimized masks at each acceleration factor. The U-Net was used only in the mask optimization algorithm for efficiency and a post-trained MoDL network provided better final image quality.

### D. Performance Metrics

To evaluate the quality of reconstructed images, we used normalized root mean squared error (NRMSE), structural similarity index (SSIM) [54], and peak signal-to-noise ratio (PSNR) as the metrics. These metrics assess the similarity between the ground truth and the reconstructed images. Lower NRMSE, higher SSIM and PSNR values suggest better reconstruction quality. All the metrics were evaluated on the central  $320 \times 320$  portion of the image. Their mathematical expressions can be given by

$$\text{NRMSE}(\mathbf{x}, \hat{\mathbf{x}}) = \frac{\|\mathbf{x} - \hat{\mathbf{x}}\|_2}{\|\mathbf{x}\|_2}, \quad (9)$$

$$\text{SSIM}(\mathbf{x}, \hat{\mathbf{x}}) = \frac{(2\mu_{\mathbf{x}}\mu_{\hat{\mathbf{x}}} + c_1)(2\sigma_{\mathbf{x}\hat{\mathbf{x}}} + c_2)}{(\mu_{\mathbf{x}}^2 + \mu_{\hat{\mathbf{x}}}^2 + c_1)(\mu_{\mathbf{x}}^2 + \mu_{\hat{\mathbf{x}}}^2 + c_2)}, \quad (10)$$

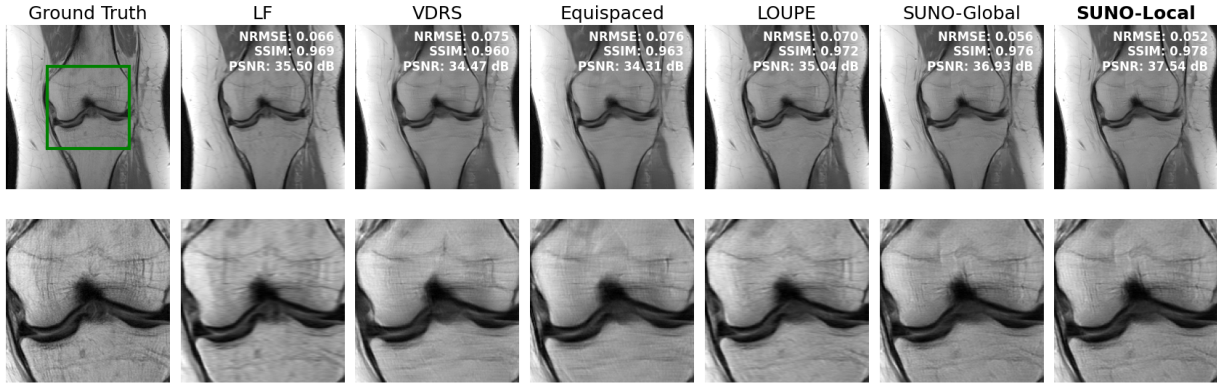


Fig. 4: Reconstructed images using MoDL network at  $4\times$  acceleration factor for a testing slice. The second row shows the zoom-in images from the area inside the green rectangle which shows that both the SUNO-Local and SUNO-Global approach outperforms the rest in terms of visual quality and better preserves structural detail.

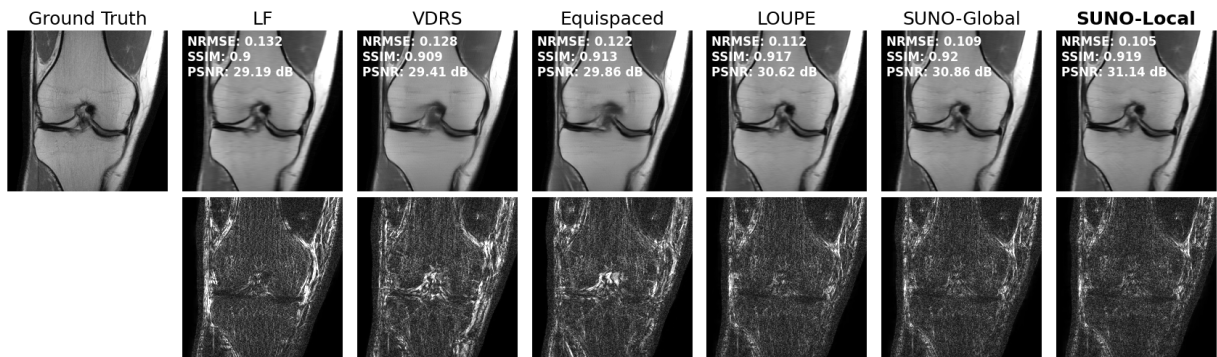


Fig. 5: Reconstructed images using MoDL network at  $8\times$  acceleration factor for a testing slice. The second row shows the error maps which show that both the SUNO-Local and SUNO-Global outperform the rest in terms of visual quality and preserve structural details better. The error images (magnitudes) shown are in the range  $[0, 0.1]$

$$\text{PSNR}(\mathbf{x}, \hat{\mathbf{x}}) = 10 \log_{10} \frac{\max(|\mathbf{x}|)^2 d}{\|\mathbf{x} - \hat{\mathbf{x}}\|_2^2}, \quad (11)$$

where  $\mathbf{x}$  and  $\hat{\mathbf{x}}$  are the ground truth and reconstructed images, respectively, and  $d$  is the total number of pixels in the image.  $\mu_{\mathbf{x}}$  and  $\mu_{\hat{\mathbf{x}}}$  are the mean of images  $\mathbf{x}$  and  $\hat{\mathbf{x}}$ ,  $\sigma_{\mathbf{x}}^2$  and  $\sigma_{\hat{\mathbf{x}}}^2$  are their respective variances and  $\sigma_{\mathbf{x}\hat{\mathbf{x}}}$  is the covariance between them.  $c_1$  and  $c_2$  are two constants dependent on the range of pixel values.

## IV. RESULTS

### A. Studies on the fastMRI Multi-Coil Knee Dataset

In this section, we show the result of applying our optimized scan-adaptive SUNO masks on the fastMRI multi-coil knee dataset at  $4\times$  and  $8\times$  acceleration factors. We compare the quality of the reconstructed images using our optimized masks with the other baseline masks described in section III-B. Figure 4 show the reconstructed images (along with zoom-ins over a region of interest) using SUNO mask along with low-frequency, VDRS, equispaced, and LOUPE masks at  $4\times$  acceleration factor, respectively. It is clear from the figure that the proposed SUNO approach (both global and local) gives better reconstructed images compared to other baselines

in terms of NRMSE, SSIM, and PSNR metrics. The zoom-ins also show that the reconstructed image using the SUNO mask preserves the fine structural detail present in the ground truth. Figure 5 shows the reconstructed and error images at  $8\times$  acceleration factor using the SUNO-Local and SUNO-Global approaches along with the other baselines. The error images show the least reconstructed error using the SUNO approach (both global and local) compared to other baselines. Table II shows the mean and standard deviation values of NRMSE, SSIM, and PSNR metrics of reconstructed images using different masks learned over all test cases. From the table, we can see that the proposed SUNO-Local and SUNO-Global approaches outperform the rest on average over the entire test set.

### B. Applicability to Different Anatomies

To test the applicability of our proposed scan-adaptive sampling prediction approach on different anatomies, we also optimized masks using the proposed training pipeline on the fastMRI multi-coil brain dataset. Then using the nearest neighbor search, the masks were predicted at test time and the performance of these learned SUNO masks was compared with the other baselines - low-frequency, VDRS, equispaced, and LOUPE masks.

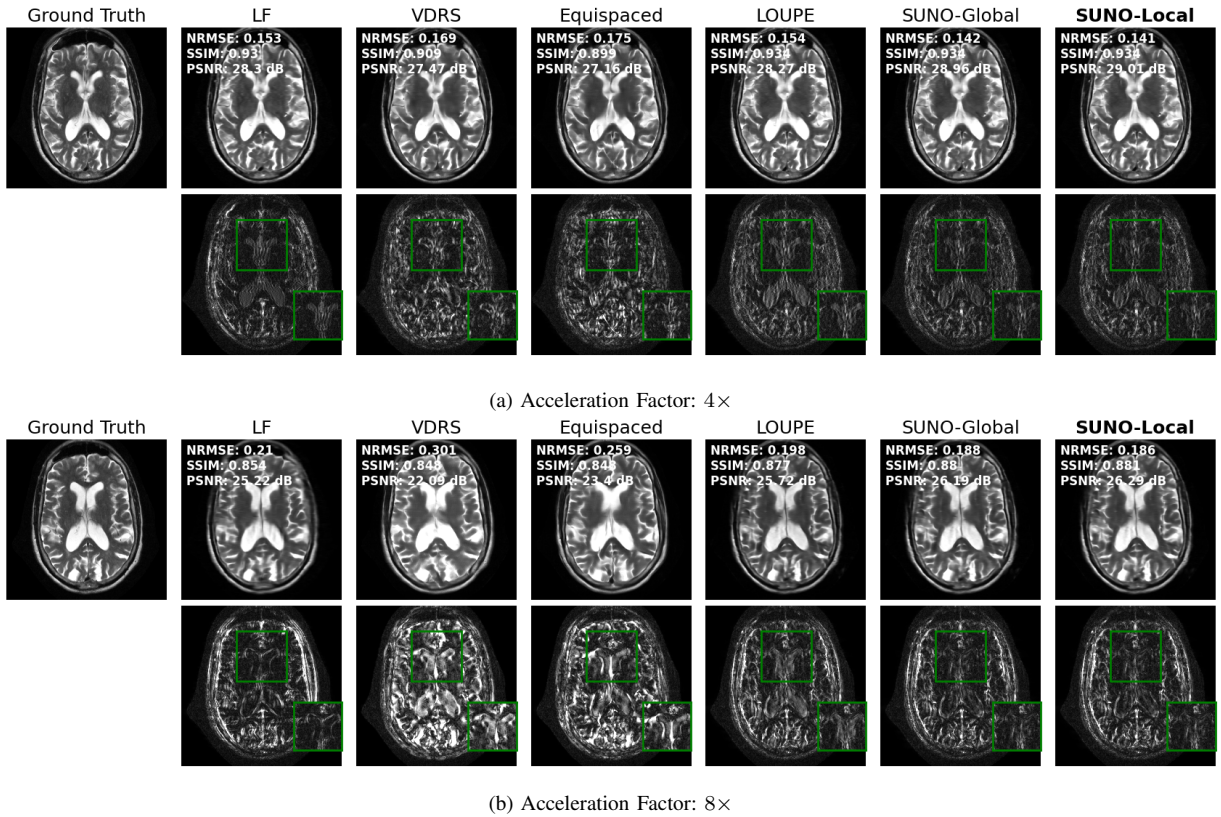


Fig. 6: Reconstructed and error images using different undersampling patterns using MoDL reconstructor (two-channel) on fastMRI brain dataset at a) 4× and b) 8× acceleration factors. The green rectangle shows the zoomed-in portions in the error image. The proposed SUNO approach perform better than other baselines in terms of NRMSE, SSIM, and PSNR metrics for both acceleration factors.

Figure 6 shows the reconstructed and error images using a brain testing slice for 4× and 8× acceleration factors. The figure shows that the optimized scan adaptive SUNO masks outperform the other baseline masks in terms of NRMSE, SSIM, and PSNR metrics for both acceleration factors. The error images also show less reconstruction error for the SUNO local and global approaches. The mean and standard deviation values of the reconstruction metrics using different masks learned over all test cases are mentioned in Table II. From the table, we can see that the proposed SUNO-Local and SUNO-Global approaches outperform all baselines.

### C. Comparison with the Oracle Case

In this section, we compare the performance of oracle masks optimized directly on the test slices (using the sampling optimization with a fixed reconstructor) with the ones predicted from the nearest neighbor search (SUNO masks). Table III gives a comparison of the oracle and SUNO masks for the fastMRI knee dataset. We observe that the oracle-optimized masks perform better than the SUNO mask for both acceleration factors as expected. This is because the oracle mask was optimized for the particular test scan (scan-adaptive) while the SUNO mask uses the mask optimized on the nearest neighbor training scan. Hence, the oracle masks perform slightly better in general. However, we want to emphasize that estimating the oracle masks requires access to the ground truth, making it infeasible at test time.

### D. Ablation Study - Convergence and Choice of Parameters for the Sampling Optimization Algorithm

In this section, we show the effect of changing different parameters for running the ICD sampling optimization (Algorithm 1) on the optimized SUNO masks for the fastMRI multi-coil knee dataset.

1) *Effect of initialization*: In this section, we explore the effect of changing the initial mask used for the sampling pattern optimization - VDRS [8] and LOUPE [38] mask. The algorithm when started with a particular mask and given a choice of reconstruction method and loss used could give different solutions. Table IV lists the performance metrics for the images reconstructed using SUNO masks optimized from a) VDRS mask and b) LOUPE mask with the MoDL reconstruction network. Figure 7 shows one such example of the reconstructed images obtained from SUNO masks initialized using LOUPE and VDRS masks. From the results, we observe that the sampling optimization initialized with the LOUPE mask results in a better reconstruction compared to when it is initialized with a VDRS mask. Since the LOUPE mask is already optimized for multiple training scans (population adaptive), it acts as a better initial point for starting the sampling optimization. The algorithm further optimizes the LOUPE mask for scan-specific details, hence we get better performance with it compared to LOUPE on test scans.

2) *Effect of reconstruction method*: This section shows the effect of the reconstruction method used inside the Algo-

Dataset	Mask	4x			8x		
		NRMSE ↓	SSIM ↑	PSNR (dB) ↑	NRMSE ↓	SSIM ↑	PSNR (dB) ↑
Knee	LF	0.134 ± 0.066	0.929 ± 0.031	30.59 ± 3.05	0.203 ± 0.064	0.884 ± 0.041	27.34 ± 2.77
	VDRS	0.137 ± 0.051	0.920 ± 0.031	31.08 ± 2.50	0.208 ± 0.065	0.873 ± 0.038	26.66 ± 2.26
	Equispaced	0.127 ± 0.050	0.927 ± 0.031	30.67 ± 2.58	0.201 ± 0.067	0.878 ± 0.042	27.00 ± 2.27
	LOUPE	0.116 ± 0.049	0.938 ± 0.028	31.63 ± 2.81	0.178 ± 0.072	0.900 ± 0.039	28.34 ± 2.78
	SUNO-Global	0.114 ± 0.046	0.940 ± 0.029	31.74 ± 2.85	0.172 ± 0.065	0.901 ± 0.039	28.54 ± 2.61
	SUNO-Local	<b>0.110 ± 0.045</b>	<b>0.941 ± 0.029</b>	<b>32.07 ± 2.83</b>	<b>0.170 ± 0.066</b>	<b>0.902 ± 0.039</b>	<b>28.70 ± 2.66</b>
Brain	LF	0.154 ± 0.046	0.956 ± 0.014	30.22 ± 2.57	0.236 ± 0.066	0.894 ± 0.042	26.58 ± 1.98
	VDRS	0.175 ± 0.052	0.938 ± 0.019	29.28 ± 2.20	0.271 ± 0.071	0.893 ± 0.039	25.35 ± 2.24
	Equispaced	0.156 ± 0.038	0.941 ± 0.020	29.93 ± 2.01	0.259 ± 0.051	0.891 ± 0.038	25.63 ± 1.68
	LOUPE	0.119 ± 0.033	0.962 ± 0.014	32.38 ± 2.26	0.202 ± 0.046	0.918 ± 0.033	27.82 ± 1.62
	SUNO-Global	0.117 ± 0.031	0.962 ± 0.013	32.53 ± 2.20	0.198 ± 0.046	0.918 ± 0.032	27.98 ± 1.59
	SUNO-Local	<b>0.115 ± 0.030</b>	<b>0.963 ± 0.012</b>	<b>32.59 ± 2.17</b>	<b>0.194 ± 0.040</b>	<b>0.919 ± 0.032</b>	<b>28.13 ± 1.40</b>

TABLE II: Distribution of NRMSE, SSIM, and PSNR values for reconstructed images for knee and brain datasets at 4x and 8x acceleration factors using various masks. SUNO-Local and SUNO-Global outperform the rest at both acceleration factors. The values displayed are mean ± std.

Acceleration Factor	4x	8x
Oracle	<b>0.110/0.941/32.07</b>	<b>0.149/0.902/29.60</b>
SUNO	0.114/0.940/31.74	0.172/0.901/28.54

TABLE III: Comparison of the oracle and SUNO masks on the fastMRI knee dataset on the test cases. The values shown are mean NRMSE/SSIM/PSNR.

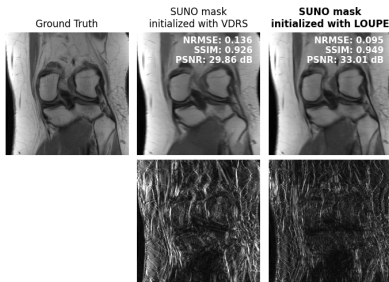


Fig. 7: Comparing reconstructed images using SUNO masks initialized from LOUPE and VDRS masks at 8x acceleration factor.

gorithm 1 on the quality of optimized SUNO masks. The algorithm works for any choice of reconstruction method, e.g., compressed sensing (CS) or a pre-trained deep learning model (e.g., U-Net, MoDL, or VarNet [24], [25]). In this paper, we show masks optimized using two such methods - U-Net and MoDL and compare the reconstructed images using these masks. Figure 8 shows the U-Net and MoDL reconstructed images using two optimized masks: one that used U-Net as the reconstruction model in the sampling optimization algorithm and the other with MoDL. The figure shows that we get the best reconstruction when a better reconstructor (i.e., MoDL network) is used both as the reconstruction model inside the sampling optimization and as the final reconstructor method.

### E. Computational Complexity of Proposed Approaches

This section discusses the time complexity of our proposed algorithms: 1) the sampling optimization algorithm and 2) the nearest neighbor search.

1) *Complexity of Algorithm 1*: In this section, we show the effect of different parameters on the run time required for the sampling pattern optimization algorithm. The algorithm learns a unique mask for each training scan and slice and as a result, an important thing to consider as part of the training pipeline

Initial Mask Chosen	NRMSE	SSIM	PSNR
VDRS	0.164	0.896	28.45
LOUPE	<b>0.142</b>	<b>0.903</b>	<b>29.78</b>

TABLE IV: Mean values of reconstruction metrics for masks initialized with VDRS and LOUPE at an 8x acceleration factor, evaluated over 50 test cases. The sampling optimization when initialized with the LOUPE mask results in better reconstruction quality.

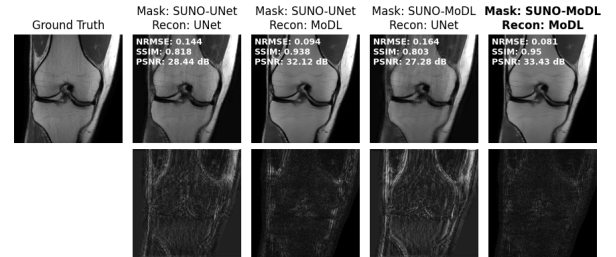


Fig. 8: Comparison of reconstructed images from masks optimized using 1) U-Net and 2) MoDL as the reconstruction model. For each mask, the reconstructed images using both the U-Net and MoDL network is shown.

is the computational complexity of the algorithm. Some of the parameters affecting runtime for the algorithm 1 are the reconstruction method that is run repeatedly while moving sampling lines or phase encodes in the mask and the underlying undersampling factor. Table V shows the dependence of the runtime on both these parameters. It is clear from the table that the sampling optimization algorithm using a U-Net reconstruction model results in a lower runtime compared to running the algorithm using a MoDL reconstructor. This is because the MoDL reconstructor uses multiple unrolling of the denoiser and the CG block [28].

Reconstructor Used	4x	8x
U-Net	25.3	13.3
MoDL	52.1	28.6

TABLE V: Time required (minutes) for running one pass of Algorithm 1 (offline). Separate times are shown for U-Net and MoDL reconstructors at 4x and 8x acceleration factors. The algorithm was run on an NVIDIA RTX A5000 GPU with 24 GB RAM.

2) *Cost of Nearest Neighbor Search*: In this section, we discuss the time complexity of neighbor search and local



MoDL network training. Table VI shows the time involved in finding the nearest neighbors for selecting the SUNO mask from the training set, the time taken to find neighbors for local network training, and the corresponding local network training time (with 30 images). Note that all these steps (except selecting the nearest neighbor mask) are post-processing (i.e., after the initial scan of low-frequency phase encoding lines has been collected). Also, the testing/inference time with the trained local MoDL network is the same as for the pre-trained (global) MoDL since the network architecture remains the same.

Procedure	Nearest Neighbor Mask Selection	Neighborhood Selection for Local Training	Local Network Training	Inference
Time	0.85	0.85	400	1.53

**TABLE VI:** Time taken (in seconds) for various procedures involved in the neighbor selection, network training, and inference. Local network training and inference steps are offline since they will be done after the data is acquired.

## V. DISCUSSION

We proposed a novel way of learning scan-adaptive Cartesian undersampling patterns for multi-coil MRI setting. The proposed method was shown to have better accuracy than the currently used population-based 1D Cartesian undersampling patterns in terms of NRMSE, SSIM, and PSNR metrics as well as the visual quality at 4x and 8x acceleration factors. The zoomed-in images show better features in the reconstructed images using the proposed SUNO masks compared to other baselines. The proposed method was tested on two different anatomies - knee and brain - and its generalization was indicated for different datasets. Similar to the greedy algorithm in prior work [35], the sampling optimization algorithm can be used along with any choice of reconstruction method and the loss metric, giving freedom in designing sampling patterns for different anatomies and different acceleration factors. A nearest neighbor search was used to predict the pattern at test time from the dictionary of learned patterns. Furthermore, a local network was trained in the neighborhood of the test image, yielding even better accuracy at test time than a global network trained on the whole training set.

A drawback of the current method is the time-consuming process of learning scan-adaptive sampling patterns on the whole training set. More work is required to make the optimization process efficient and faster to make this approach more feasible. However, since this sampling optimization is part of the offline training module, it does not affect the acquisition and sampling prediction at test time which is 0.85 seconds in our experiments.

## VI. CONCLUSION

In this work, we proposed a novel MRI sampling prediction algorithm for multi-coil MRI that estimates a collection of scan-adaptive sampling patterns and a reconstruction network trained on those patterns alternately, at the training time. The proposed algorithm was validated on the publicly available

fastMRI knee and brain dataset and was shown to have better reconstruction accuracy than currently used Cartesian undersampling patterns. This study demonstrated the advantages of employing scan-adaptive masks by providing evidence that they are more effectively tailored to individual patients than population-adaptive masks. We also showed the dependence of the learned sampling patterns on acceleration factors, the initialization of the sampling algorithm, and the reconstruction method used. Future work will include employing deep image prior or other scan-adaptive MRI reconstructions in our framework, extending the approach to cardiac MRI, and/or predicting sparse views for X-ray CT reconstruction.

## VII. ACKNOWLEDGMENTS

The authors would like to acknowledge Dr. Maryam Sayadi, Michigan State University for her inputs throughout the project. The authors also acknowledge Evan Bell and Shijun Liang from Michigan State University, and Zhishen Huang from Amazon Inc. for useful discussions.

## REFERENCES

- [1] Z. Liang and P.C. Lauterbur, *Principles of magnetic resonance Img.*, SPIE Optical Engineering Press Bellingham, WA, 2000.
- [2] M.A. Bernstein, K.F. King, and X.J. Zhou, *Handbook of MRI pulse sequences*, Elsevier, 2004.
- [3] J. Tsao, "Ultrafast imaging: principles, pitfalls, solutions, and applications," *Journal of Mag. Reson. Img.*, vol. 32, no. 2, pp. 252–266, 2010.
- [4] K.P. Pruessmann, "Encoding and reconstruction in parallel MRI," *NMR in Biomedicine*, vol. 19, no. 3, pp. 288–299, 2006.
- [5] L. Ying and Z. Liang, "Parallel MRI using phased array coils," *IEEE Signal Processing Magazine*, vol. 27, no. 4, pp. 90–98, 2010.
- [6] A. Deshmane, V. Gulani, M.A. Griswold, and N. Seiberlich, "Parallel MR img.," *Journal of Mag. Reson. Img.*, vol. 36, no. 1, pp. 55–72, 2012.
- [7] D.L. Donoho, "Compressed sensing," *IEEE Trans. on information theory*, vol. 52, no. 4, pp. 1289–1306, 2006.
- [8] M. Lustig, D. Donoho, and J.M. Pauly, "Sparse MRI: The application of compressed sensing for rapid MR img.," *Magn. Reson. in Med.*, vol. 58, no. 6, pp. 1182–1195, 2007.
- [9] E.J. Candes and T. Tao, "Near-optimal signal recovery from random projections: Universal encoding strategies?," *IEEE Trans. on information theory*, vol. 52, no. 12, pp. 5406–5425, 2006.
- [10] E. Candes and J. Romberg, "Sparsity and incoherence in compressive sampling," *Inverse problems*, vol. 23, no. 3, pp. 969, 2007.
- [11] M. Lustig, D.L. Donoho, J.M. Santos, and J.M. Pauly, "Compressed sensing MRI," *IEEE signal processing magazine*, vol. 25, no. 2, pp. 72–82, 2008.
- [12] Z. Wang and G.R. Arce, "Variable density compressed image sampling," *IEEE Trans. on image processing*, vol. 19, no. 1, pp. 264–270, 2009.
- [13] M. Murphy, M. Alley, J. Demmel, K. Keutzer, S. Vasanawala, and M. Lustig, "Fast H-spirit compressed sensing parallel imaging MRI: scalable parallel implementation and clinically feasible runtime," *IEEE Trans. on Med. Img.*, vol. 31, no. 6, pp. 1250–1262, 2012.
- [14] E. Levine, B. Daniel, S. Vasanawala, B. Hargreaves, and M. Saranathan, "3d cartesian MRI with compressed sensing and variable view sharing using complementary poisson-disc sampling," *Magn. Reson. in Med.*, vol. 77, no. 5, pp. 1774–1785, 2017.
- [15] J.P. Haldar, D. Hernando, and Z. Liang, "Compressed-sensing MRI with random encoding," *IEEE Trans. on Med. Img.*, vol. 30, no. 4, pp. 893–903, 2010.
- [16] S. Ravishanker and Y. Bresler, "MR image reconstruction from highly undersampled k-space data by dictionary learning," *IEEE Trans. on Med. Img.*, vol. 30, no. 5, pp. 1028–1041, 2010.
- [17] S.G. Lingala and M. Jacob, "Blind compressive sensing dynamic MRI," *IEEE Trans. on Med. Img.*, vol. 32, no. 6, pp. 1132–1145, 2013.
- [18] X. Qu, Y. Hou, F. Lam, D. Guo, J. Zhong, and Z. Chen, "Magnetic resonance image reconstruction from undersampled measurements using a patch-based nonlocal operator," *Med. image analysis*, vol. 18, no. 6, pp. 843–856, 2014.

- [19] Z. Zhan, J. Cai, D. Guo, Y. Liu, Z. Chen, and X. Qu, "Fast multiclass dictionaries learning with geometrical directions in MRI reconstruction," *IEEE Trans. on bioMed. engineering*, vol. 63, no. 9, pp. 1850–1861, 2015.
- [20] S. Ravishankar and Y. Bresler, "Learning sparsifying transforms," *IEEE Trans. on Signal Processing*, vol. 61, no. 5, pp. 1072–1086, 2012.
- [21] S. Ravishankar, J.C. Ye, and J.A. Fessler, "Image reconstruction: From sparsity to data-adaptive methods and machine learning," *Proceedings of the IEEE*, vol. 108, no. 1, pp. 86–109, 2019.
- [22] O. Ronneberger, P. Fischer, and T. Brox, "U-Net: Convolutional networks for biomed. image segmentation," in *International Conference on Med. image computing and computer-assisted intervention*. Springer, 2015, pp. 234–241.
- [23] C.M. Hyun, H.P. Kim, S.M. Lee, S. Lee, and J.K. Seo, "Deep learning for undersampled MRI reconstruction," *Physics in Medicine & Biology*, vol. 63, no. 13, pp. 135007, 2018.
- [24] K. Hammernik, T. Klatzer, E. Kobler, M.P. Recht, D.K. Sodickson, T. Pock, and F. Knoll, "Learning a variational network for reconstruction of accelerated MRI data," *Magn. Reson. in Med.*, vol. 79, no. 6, pp. 3055–3071, 2018.
- [25] A. Sriram, J. Zbontar, T. Murrell, A. Defazio, C.L. Zitnick, N. Yakubova, F. Knoll, and P. Johnson, "End-to-end variational networks for accelerated MRI reconstruction," in *Med. Image Computing and Computer Assisted Intervention—MICCAI 2020: 23rd International Conference, Lima, Peru, October 4–8, 2020, Proceedings, Part II 23*. Springer, 2020, pp. 64–73.
- [26] J. Sun, H. Li, Z. Xu, et al., "Deep ADMM-Net for compressive sensing MRI," *Advances in neural information processing systems*, vol. 29, 2016.
- [27] M. Mardani, E. Gong, J.Y. Cheng, S. Vasanawala, G. Zaharchuk, M. Alley, N. Thakur, S. Han, W. Dally, J.M. Pauly, et al., "Deep generative adversarial networks for compressed sensing automates MRI," *arXiv preprint arXiv:1706.00051*, 2017.
- [28] H.K. Aggarwal, M.P. Mani, and M. Jacob, "MoDL: Model-based deep learning architecture for inverse problems," *IEEE Trans. on Med. Img.*, vol. 38, no. 2, pp. 394–405, 2018.
- [29] S. Ravishankar and Y. Bresler, "Adaptive sampling design for compressed sensing MRI," in *2011 Annual International Conference of the IEEE Engineering in Medicine and Biology Society*. IEEE, 2011, pp. 3751–3755.
- [30] F. Knoll, C. Clason, C. Diwoky, and R. Stollberger, "Adapted random sampling patterns for accelerated MRI," *Magnetic resonance materials in physics, biology and medicine*, vol. 24, pp. 43–50, 2011.
- [31] J. Vellagoundar and R.R. Machireddy, "A robust adaptive sampling method for faster acquisition of MR images," *Magnetic resonance Img.*, vol. 33, no. 5, pp. 635–643, 2015.
- [32] Y. Zhang, B.S. Peterson, G. Ji, and Z. Dong, "Energy preserved sampling for compressed sensing MRI," *Computational and mathematical methods in medicine*, vol. 2014, no. 1, pp. 546814, 2014.
- [33] J.P. Haldar and D. Kim, "OEDIPUS: An experiment design framework for sparsity-constrained MRI," *IEEE Trans. on Med. Img.*, vol. 38, no. 7, pp. 1545–1558, 2019.
- [34] M. Seeger, H. Nickisch, R. Pohmann, and Bernhard Schölkopf, "Optimization of k-space trajectories for compressed sensing by bayesian experimental design," *Magn. Reson. in Med.*, vol. 63, no. 1, pp. 116–126, 2010.
- [35] B. Gözcü, R. K. Mahabadi, Y. Li, E. Ilıcak, T. Cukur, J. Scarlett, and V. Cevher, "Learning-based compressive MRI," *IEEE Trans. on Med. Img.*, vol. 37, no. 6, pp. 1394–1406, 2018.
- [36] B. Gözcü, T. Sanchez, and V. Cevher, "Rethinking sampling in parallel MRI: A data-driven approach," in *2019 27th European Signal Processing Conference (EUSIPCO)*. IEEE, 2019, pp. 1–5.
- [37] T. Sanchez, B. Gözcü, R. van Heeswijk, A. Eftekhari, E. Ilıcak, T. Çukur, and V. Cevher, "Scalable learning-based sampling optimization for compressive dynamic MRI," in *2020 IEEE International Conference on Acoustics, Speech and Signal Processing (ICASSP)*. IEEE, 2020, pp. 8584–8588.
- [38] C.D. Bahadir, A.Q. Wang, A.V. Dalca, and M.R. Sabuncu, "Deep-learning-based optimization of the under-sampling pattern in MRI," *IEEE Trans. on Computational Img.*, vol. 6, pp. 1139–1152, 2020.
- [39] J. Zhang, H. Zhang, A. Wang, Q. Zhang, M. Sabuncu, P. Spincemaille, T.D. Nguyen, and Y. Wang, "Extending LOUPE for k-space under-sampling pattern optimization in multi-coil MRI," in *Machine Learning for Med. Image Reconstruction: Third International Workshop, MLMIR 2020, Lima, Peru, October 8, 2020, Proceedings 3*. Springer, 2020, pp. 91–101.
- [40] H.K. Aggarwal and M. Jacob, "J-MoDL: Joint model-based deep learning for optimized sampling and reconstruction," *IEEE journal of selected topics in signal processing*, vol. 14, no. 6, pp. 1151–1162, 2020.
- [41] F. Sherry, M. Benning, J.C. De los Reyes, M.J. Graves, G. Maierhofer, G. Williams, Carola-Bibiane Schönlieb, and Matthias J Ehrhardt, "Learning the sampling pattern for MRI," *IEEE Trans. on Med. Img.*, vol. 39, no. 12, pp. 4310–4321, 2020.
- [42] M.V. Zibetti, G.T. Herman, and R.R. Regatte, "Fast data-driven learning of parallel MRI sampling patterns for large scale problems," *Scientific Reports*, vol. 11, no. 1, pp. 19312, 2021.
- [43] M.V.W. Zibetti, F. Knoll, and R.R. Regatte, "Alternating learning approach for variational networks and undersampling pattern in parallel MRI applications," *IEEE Trans. on Computational Img.*, vol. 8, pp. 449–461, 2022.
- [44] Z. Huang and S. Ravishankar, "Single-pass object-adaptive data under-sampling and reconstruction for MRI," *IEEE Trans. on Computational Img.*, vol. 8, pp. 333–345, 2022.
- [45] C. Alkan, M. Mardani, C. Liao, Z. Li, S.S. Vasanawala, and J.M. Pauly, "Autosamp: Autoencoding k-space sampling via variational information maximization for 3D MRI," *IEEE Trans. on Med. Img.*, 2024.
- [46] L. Pineda, S. Basu, A. Romero, R. Calandra, and M. Drozdal, "Active MR k-space sampling with reinforcement learning," in *Med. Image Computing and Computer Assisted Intervention—MICCAI 2020: 23rd International Conference, Lima, Peru, October 4–8, 2020, Proceedings, Part II 23*. Springer, 2020, pp. 23–33.
- [47] T. Bakker, H. van Hoof, and M. Welling, "Experimental design for MRI by greedy policy search," *Advances in Neural Information Processing Systems*, vol. 33, pp. 18954–18966, 2020.
- [48] T. Yin, Z. Wu, H. Sun, A.V. Dalca, Y. Yue, and K.L. Bouman, "End-to-end sequential sampling and reconstruction for MR img.," in *Proceedings of the Machine Learning for Health Conference*, 2021.
- [49] T. Weiss, O. Senouf, S. Vedula, O. Michailovich, M. Zibulevsky, and A. Bronstein, "Pilot: Physics-informed learned optimized trajectories for accelerated mri," *arXiv preprint arXiv:1909.05773*, 2019.
- [50] C. Lazarus, P. Weiss, N. Chauffert, F. Mauconduit, L. El Gueddari, C. Destrieux, I. Zemmoura, A. Vignaud, and P. Ciuciu, "Sparkling: variable-density k-space filling curves for accelerated t2\*-weighted mri," *Magn. Reson. in Med.*, vol. 81, no. 6, pp. 3643–3661, 2019.
- [51] GR Chaithya, P. Weiss, G. Daval-Frérôt, A. Massire, A. Vignaud, and P. Ciuciu, "Optimizing full 3d sparkling trajectories for high-resolution magnetic resonance imaging," *IEEE Transactions on Medical Imaging*, vol. 41, no. 8, pp. 2105–2117, 2022.
- [52] G. Wang, T. Luo, J. Nielsen, D.C. Noll, and J.A. Fessler, "B-spline parameterized joint optimization of reconstruction and k-space trajectories (BJORK) for accelerated 2D MRI," *IEEE Trans. on Med. Img.*, vol. 41, no. 9, pp. 2318–2330, 2022.
- [53] G. Wang, J. F. Nielsen, J. A. Fessler, and D. C. Noll, "Stochastic optimization of three-dimensional non-cartesian sampling trajectory," *Magn. Reson. in Med.*, vol. 90, no. 2, pp. 417–431, 2023.
- [54] Z. Wang, A.C. Bovik, H.R. Sheikh, and E.P. Simoncelli, "Image quality assessment: from error visibility to structural similarity," *IEEE Trans. on image processing*, vol. 13, no. 4, pp. 600–612, 2004.
- [55] S. Liang, A. Lahiri, and S. Ravishankar, "Adaptive local neighborhood-based neural networks for MR image reconstruction from undersampled data," *IEEE Trans. on Computational Img.*, 2024.
- [56] S. Gautam, A. Li, and S. Ravishankar, "Patient-adaptive and learned MRI data undersampling using neighborhood clustering," in *2024 IEEE International Conference on Acoustics, Speech and Signal Processing (ICASSP)*. IEEE, 2024, pp. 2081–2085.
- [57] J. Zbontar, F. Knoll, A. Sriram, T. Murrell, Z. Huang, M.J. Muckley, A. Defazio, R. Stern, P. Johnson, M. Bruno, et al., "fastMRI: An open dataset and benchmarks for accelerated MRI," *arXiv preprint arXiv:1811.08839*, 2018.
- [58] F. Knoll, J. Zbontar, A. Sriram, M.J. Muckley, M. Bruno, A. Defazio, M. Parente, K.J. Geras, J. Katsnelson, H. Chandarana, et al., "fastMRI: A publicly available raw k-space and dicom dataset of knee images for accelerated MR image reconstruction using machine learning," *Radiology: Artificial Intelligence*, vol. 2, no. 1, pp. e190007, 2020.
- [59] M. Uecker, P. Lai, M.J. Murphy, P. Virtue, M. Elad, J.M. Pauly, S.S. Vasanawala, and M. Lustig, "ESPIRiT — an eigenvalue approach to autocalibrating parallel MRI: where SENSE meets GRAPPA," *Magn. Reson. in Med.*, vol. 71, no. 3, pp. 990–1001, 2014.
- [60] S. Yu, B. Park, and J. Jeong, "Deep iterative down-up CNN for image denoising," in *Proceedings of the IEEE/CVF conference on computer vision and pattern recognition workshops*, 2019.
- [61] D.P. Kingma and J. Ba, "Adam: A method for stochastic optimization," *arXiv preprint arXiv:1412.6980*, 2014.